



ORIGINAL ARTICLE

Enhanced alcohol and H₂O adsorption and separation performances by introducing pyridyl ligand in a MOF



Chenxu Zhang^{a,1}, Mingming Zhai^{a,1}, Kangning Xie^{a,1}, Yingchao Wang^a,
Xiuyuan Li^b, Juan Liu^a, Yuanzhe Li^a, Yanfei Hu^c, Erping Luo^{a,*}, Chi Tang^{a,*}

^a Shaanxi Provincial Key Laboratory of Bioelectromagnetic Detection and Intelligent Perception, School of Biomedical Engineering, Air Force Medical University, Xi'an 710032, PR China

^b Shaanxi Key Laboratory of Optoelectronic Functional Materials and Devices, School of Materials Science and Chemical Engineering, Xi'an Technological University, Xi'an 710021, PR China

^c Department Wide Bandgap Semiconductor Technology Disciplines State Key Laboratory, Institution School of Microelectronics, Xidian University, Xi'an 710071, PR China

Received 14 March 2022; accepted 19 July 2022

Available online 22 July 2022

KEYWORDS

MOFs;
Adsorption;
GCMC simulations;
IAST

Abstract MOFs (Metal-Organic Framework), as promising crystalline materials of adsorption and separation, has been the subject of many recent investigations. However, the H₂O stability of MOFs and the variation of adsorption selectivity in humid environments largely hinder attempts as excellent adsorbents in numerous scenarios. This study employs hydro-thermal synthesis [Cd_{0.5}(DPETA)_{0.5}]_n using 2,3',5,5'-Diphenyl tetracarboxylic acid (DPETA) and Cd(NO₃)₂·4H₂O as ligands and metal ions, respectively. And it is modified by adding auxiliary ligands 4-4'-bipyridyl (bpy) and 1,2-bis (4-pyridyl) ethylene(bpe) to obtain [Cd_{1.5}bpy₂(DPETA)]_n and [Cd₂bpe₂(DPETA)]_n. The phase purity of the MOFs is examined using PXRD and FT-IR spectrum. The adsorption capacities of three MOFs are tested separately for water, ethanol and methanol using vapor adsorption. Their adsorption conformations and hydrogen bond lengths are also calculated by the GCMC method. The adsorption selection ratios of methanol and ethanol are deduced in combination with the IAST method under three components of water, methanol and ethanol. The results shows a methanol/ethanol adsorption separation ratio of 45 for [Cd_{1.5}bpy₂(-

Abbreviations: MOFs, Metal-Organic Frameworks; GCMC, Grand Canonical Monte Carlo; IAST, Ideal Adsorbed Solution Theory

* Corresponding authors.

E-mail addresses: luoeping@fmmu.edu.cn (E. Luo), tangchi@fmmu.edu.cn (C. Tang).

¹ These authors contributed to the work equally and should be regarded as co-first authors.

Peer review under responsibility of King Saud University.



DPETA)]_n at 297 K, which is consistent with the of GCMC demonstrated. These results suggest that the methanol/ethanol adsorption selectivity ratio can be improved by increasing the adsorption force on methanol through by adding of auxiliary pyridyl ethylene. It can be used for efficient methanol/ethanol separation in humid environments.

© 2022 The Author(s). Published by Elsevier B.V. on behalf of King Saud University. This is an open access article under the CC BY-NC-ND license (<http://creativecommons.org/licenses/by-nc-nd/4.0/>).

1. Introduction

MOFs are crystalline materials with highly ordered structures formed by individual metal cations or metal clusters linked by multi-dentate organic ligands. Due to their highly elastic properties, MOFs with different design and properties can be synthesized by modifying organic ligands, which are widely used in energy, environmental, biomedical, detection, catalysis and other fields (Guan et al., 2020; Li et al., 2021; Liu et al., 2020; Lu et al., 2022). It was enthusiastically pursued in the past 20 years. According to Web of Science data, there are more than 6,000 studies on MOFs materials in 2021, covering many disciplines such as chemistry, energy, life sciences, pharmaceuticals, and mechanics. MOFs materials are ideal for gas storage, gas separation, and sensing and detection because of the low density, large specific surface area, adjustable pore diameters, and flexible structure (Yuan et al., 2016; Deng et al., 2019; Schüttrumpf et al., 2017).

In toxic vapor separation and fuel purification, it is often necessary to sort out specific products under the conditions of mixing multiple alcohols with water vapor gas (Fomkin and Petukhova, 2020). Alcohol vapor separation has always been a research hotspot in the chemical industry (Zheng et al., 2014; do Thi et al., 2020). With the increasing awareness of environmental protection, the traditional constant boiling and extractive distillation processes not only consume a lot of energy, but also often use toxic azeotropes (Yuan et al., 2016). Therefore, a clean alcohol separation process is urgently needed. MOFs material as pore filler to prepare membrane modules for alcohol permeation vaporization is 30–40 % more energy-efficient than azeotropic distillation. And almost no liquid flooding, fog foam entrapment and other serious problems that conventional distillation processes (Sander and Soukup, 1988; Selvaraj and Banat, 2019). This research is in its initial stage and has great potential for development. However, as an alternative ideal adsorbent material for the future, the water adsorption properties and H₂O stability of MOFs have been the major limitation of their widespread diffusion.

In 2008, J. M. Castillo et al. studied the adsorption behaviour of H₂O in Cu-BCT using molecular simulations, showing that H₂O molecule has a surprising affinity for the metal atoms in this structure. This result can be applied to the separation of water from other compounds (Castillo et al., 2008). 2009, P. Küsgens et al. studied the H₂O adsorption properties and H₂O stability of the common HKUST-1 ZIF-8, MIL-101, MIL-100(Fe) and DUT-4. Their application in water adsorption is predicted in terms of stability, hydrophilicity and adsorption capacity (Küsgens et al., 2009). 2012, Schoenecker, P.M. et al. investigated the structural changes and specific surface area loss of Mg MOF-74 after water absorption by Powder X-ray Diffraction (PXRD) and N₂ adsorption experiment, revealing the intrinsic mechanism of structural collapse of

MOFs (Schoenecker et al., 2012). In 2013, DeCoste, J.B et al. investigated the degradation pattern of the three most common MOF materials at different temperature and humidity conditions within 28 days. The results indicate that the difference in water absorption is the most important reason for the secondary building unit (SBU) collapse of the MOFs materials (Decoste et al., 2013). In 2021, two MOFs with a same hexagonal channel, but present diverse porous wall environments are prepared by Xiu-Yuan Li et al. That effectively improved the adsorption of water and alcohol by introducing open site N atoms. This provides a good reference for preparing MOF materials with high water-alcohol adsorption capacity (Li et al., 2020). The stability and adsorption selectivity determine whether MOFs can become commercially viable adsorption separation materials in the future. From previous report, the N atom on pyridine group is sp² hybridized. There are more unbonded electrons remaining and the electron cloud density is larger. If the adsorption between pyridine and guest molecules is mainly by chemical reaction, the introduction of pyridine ligands increases the adsorption interaction (Wong-Ng et al., 2021). That is essential to develop MOFs with good water stability and alcohol separation properties.

In this paper, a method on the basis of 2,3',5,5'-Diphenyl tetracarboxylic acid (DPETA) is investigated to prepare MOFs and their modification by introducing the auxiliary ligands bpy and bpe. On one hand, the porosity is adjusted. On the other hand, adsorption amount of alcohols is enhanced by introducing pyridine rings and vinyl groups. Finally, the adsorption separation ratio of MOFs under multi-component conditions is adjusted. The adsorption capacity of H₂O and alcohols in the pore structures were also explored and further confirmed by Grand Canonical Monte Carlo (GCMC) simulations at molecular level for exploring adsorption properties of guests on MOFs. This is important for specifying and tailoring the crystal structure to make it a new functional material with specific applications.

2. Experiment methods

2.1. Synthesis of [Cd_{0.5}(DPETA)_{0.5}]_n (1), [Cd_{1.5}bpy₂(DPETA)]_n (2) and [Cd₂bpe₂(DPETA)]_n (3)

2.1.1. [Cd_{0.5}(DPETA)_{0.5}]_n

A sample bottle containing Cd(NO₃)₂·4H₂O (30.8 mg, 0.1 mmol), 2,3',5,5'-Diphenyl tetracarboxylic acid (17.3 mg, 0.1 mmol), DMF (2 mL) and H₂O (1 mL) was heated at 110 °C for 72 h. After forced-air cooling to 297 K, white granular crystal were obtained in 60 % yield. Anal. Calcd for C₈H₃O_{4.5}Cd_{0.5}: ω(C) = 42.27 %, ω(H) = 1.33 %, ω(O) = 31.67 %, ω(Cd) = 24.73 %. Found: ω(C) = 43.62 %, ω(H) = 1.58 %, ω(Cd) = 24.02 %.

2.1.2. [Cd_{1.5}bpy₂(DPETA)]_n

A sample bottle containing Cd(CH₃COO)₂·2H₂O (26.65 mg, 0.1 mmol), 2,3',5,5'-Diphenyl tetracarboxylic acid (17.3 mg, 0.1 mmol), 4,4'-bipyridyl (15.6 mg, 0.1 mmol) DMF (2 mL) and H₂O (0.5 mL) was heated at 110°C for 72 h. After forced-air cooling to 297 K, white granular crystals were obtained in 55 % yield. Anal. Calcd for C₃₆H₂₃Cd_{1.5}N₄O_{9.5}: ω(C) = 51.96 %, ω(H) = 2.79 %, ω(N) = 6.73 %, ω(Cd) = 20.26 %. Found: ω(C) = 52.47 %, ω(H) = 2.94 %, ω(N) = 7.43 %, ω(Cd) = 21.68 %.

2.1.3. [Cd₂bpe₂(DPETA)]_n

A sample bottle containing Cd(CH₃COO)₂·2H₂O (26.65 mg, 0.1 mmol), 2,3',5,5'-Diphenyl tetracarboxylic acid (17.3 mg, 0.1 mmol), 1,2-bis(4-pyridyl) ethylene (18.2 mg, 0.1 mmol) DMF (2 mL) and H₂O (0.5 mL) was heated at 110°C for 72 h. After forced-air cooling to 297 K, yellow block crystals were obtained in 63 % yield. Anal. Calcd for C₄₀H₂₆Cd₂N₄O₉: ω(C) = 51.58 %, ω(H) = 2.81 %, ω(N) = 6.01 %, ω(Cd) = 24.14 %. Found: ω(C) = 51.99 %, ω(H) = 3.02 %, ω(N) = 6.14 %, ω(Cd) = 24.78 %.

2.2. Characterization

All experimental reagents and solvents are commercially sourced and have not been further purified. Fourier Transform InfraRed (FT-IR) measured using Nicolet IS50 Thermofisher spectrometer in the 600–4000 cm⁻¹ region. The contents of C, H and N in MOFs determined by PerkinElmer 2400C elemental analyzer. The crystal structures and phase composition of the samples collected by a Bruker D2 Phaser Gen 2 X-ray Powder Diffraction (PXRD), with Cu Kα ray (λ = 1.5418 Å). Thermogravimetric analysis performed in a N₂ atmosphere using a Q600 SDT thermal analyzer at a heating rate of 5°C/min.

2.3. Structure of the complexes

A single crystal X-ray diffraction analysis performed at 297 K using Graphite monochromatic Mo Kα rays (λ = 0.71073 Å) on a Bruker Smart APEXII CCD detector using. The structure of the complexes was resolved using the direct method, and refined using the full-matrix least square method *F*² of SHELXTL package (Sheldrick, 2015). All the resulting non-hydrogen atoms are anisotropic refined, and the corresponding hydrogen atoms are added to the geometrically optimal position and refined by isotropic elements. Since disordered lattice water molecules could not be identified, structural refinement is handled using the SQUEEZE program of PLATON software (Spek, 2003).

2.4. Vapor adsorption studies

Measurements of low pressure (up to 1 atm) water, ethanol, and methanol adsorption isotherms collected on a fully automated Quantachrome Autosorb-iQ MP adsorption system at relative pressure. All the as-synthesized samples were soaked in CH₂Cl₂ for 48 h. The supernatant was replaced every 12 h. Before the vapor measurement, about 100 mg samples were completely desolvated by heating the CH₂Cl₂-exchanged

complexes at 353 K under a dynamic high vacuum for 24 h. Each pressure step set as 3 min during maximum equilibration time.

3. Results and discussion

3.1. MOFs structure

Single-crystal XRD analysis shows that complex **1** crystallizes in the original orthogonal system, the space group is PNMA, and the asymmetric unit consists of a Cd (II) atom and a DPETA ligand. As shown in Fig. 1(a) and (b), the Cd (II) atom was coordinated by eight carboxylate oxygen atoms from 4 DPETA ligands to furnish a oblique parallelepiped geometry. The Cd-O bond range from 2.301(3) to 2.576(2) Å, these values match with the previous research (Duan et al., 2010).

In each ligand DPETA, the dihedral angle between connected benzene rings is 90.45°, almost a right angle. The four carboxyl groups are linked to four Cd²⁺ ions in a double-dentate chelation mode. Cd1 and Cd2 form a binuclear set by bridging two carboxyl groups of a DPETA. The binuclear cluster is then connected with DPETA-1 to generate a wave layer parallel on the ac plane. Then adjacent wave layers are extended into 3D structures by DPETA-2. The structure has a one-dimensional rectangular channel with a diameter of 6.4 × 5.1 Å along the b-axis, and a solvent accessible volume of nearly 68 %.

To further understand the structure of **1**, topological analysis software TOPOS was utilized. If defining the DPETA ligands as four-connected nodes and the tetranuclear Cd(II) atom secondary building units as 4-connected nodes, the whole 3D framework can be described as a (4,4)-connected 2-nodal network with a topos symbol of {4².6³.8} (Fig. 1(d)).

The first strong peak at 6.5° is correspond to open channel of MOFs. Complex **1** is a spoke-type MOF constructed with Cd as metal node. From its topological network, there are square or diamond-shaped secondary structural units around the eight-membered ring. This unit is affected by the solvent to produce respiration. On the one hand, the [110] crystal plane spacing changes, corresponding the offset of XRD peaks (Ling et al., 2011). On the other hand, during simulated time, the channel is open by default. While in the product of experimental synthesis, the channel is closed. Therefore, red and blue diffraction peak does not exist (Sakata et al., 1979).

Similarly, single crystal XRD analysis shows that complex **2** crystallizes in a central monoclinic system with space group C2/C. Every asymmetric unit includes two Cd(II) atoms, one DPETA ligand, two 4,4'-bipyridyl and one coordinated H₂O molecules. In Fig. 2, The Cd1 atom is coordinated along an axis by four carboxyl O atoms and two bipyridine groups, resulting in a severely distorted octahedral geometry. The Cd-O bonds range from 2.343(5) to 2.547(3) Å, and the Cd-N bonds range from 2.258(4) to 2.354(3) Å.

In each DPETA, the dihedral angle of connected benzene rings is - 18.68°, which means the ligand has been further compressed and crimped. DPETA-1 and DPETA-2 are bridging with a Cd along the c axis to generate an almost planer layer on the ac plane. Then adjacent layers are extended by compressed C—O—C bond of DPETA into 3D structures.

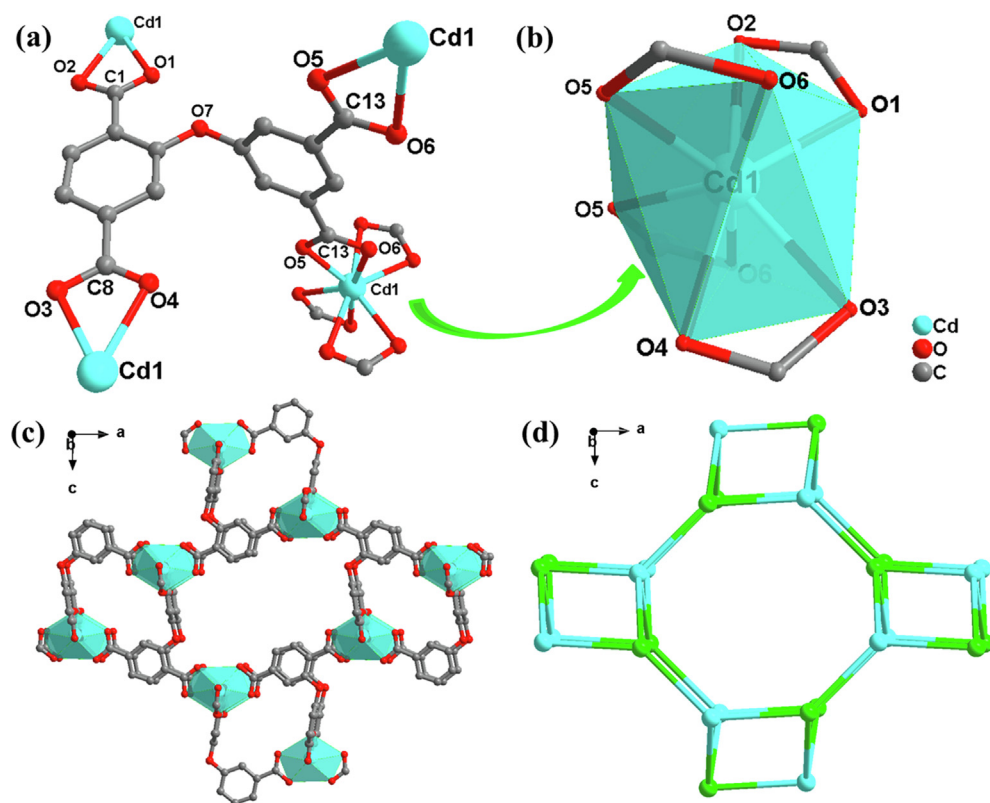


Fig. 1 (a) SBU of **1**; (b) Coordination circumstance of the Cd atom in **1**; (c) 3D framework along b axis; (d) topological network.

The structure has one-dimensional rectangular channel with a diameter of $10.1 \times 11.8 \text{ \AA}$ along the c-axis and a solvent accessible volume of nearly 68 %.

The TOPOS software is still employed to identify the topos symbol of complex **2**. The DPETA ligands as four-connected nodes. The tetranuclear Cd1 atom SBUs is 4-connected nodes and the pentanuclear Cd2 atom SBUs is 5-connected nodes. Thus, an unprecedented whole 3D framework can be described as a (3,4,5)-connected 3-nodal network with a topos symbol of $\{6^3.8^3\}\{6^3\}_2\{6^8.8^2\}_2$ (Fig. 2(d)).

Single-crystal XRD analysis of complex **3** crystallizes in the primitive monoclinic system, the space group is $P21/C$, and the asymmetric unit consists of two Cd (II) atoms, a DPETA ligand, and two 1, 2-bis (4-pyridyl) ethylene (bpe). As shown in Fig. 3(a), the Cd1 atom is coordinated by four carboxyl O atoms and two bpe nitrogen atoms. The N-Cd-N angles range from 90.321° to 91.546° , almost a right angle. The Cd-O bonds range from 2.311(3) to 2.381(3) \AA , which is shorter than **2**. And the Cd-N bonds range from 2.256(2) to 2.274(5) \AA . In each asymmetric unit, the dihedral angles connecting the DPETA and bpe (C1-O1-Cd2-N1 and C1-O2-Cd2-N4) are 61.438° and 50.942° . The two carboxyl groups links to four Cd1 ions in a double-dentate chelation mode. Cd1 and Cd2 form a binuclear cluster by bridging a bpe group along the b axis to generate an almost 2D sheet with quadrilateral lattices on the bc plane. Then neighbour layers are bonded by C—O—C of DPETA to complete a 3D noninterpenetrated microporous framework construct 1D hexagon channel with a diagonal of about 12 \AA along the a-axis, and the solvent accessible volume is close to 39.3 %, as Fig. 3(c).

As with complex **1** and **2**, the software TOPOS is still utilized. Suppose defining the DPETA ligands as 4-connected nodes and the tetranuclear Cd(II) cluster SBUs as 4-connected nodes. Thus, an unprecedented whole 3D framework can be described as a (4,4)-connected 2-nodal network with a topos symbol of $\{4.6^2.8^3\}_2\{4^2.6^2.8^2\}$ (Fig. 3(d)).

3.2. Properties

Besides Single-crystal XRD, the frameworks of complex **1**, **2** and **3** confirmed by PXRD. From the PXRD pattern of complex **1** in Fig. S1(a), the simulated data is similar to the as-synthesized sample and after gas adsorption sample. That indicates the complex **1** has a good phase purity and the basic framework remains unchanged after the vapor adsorption process.

By comparing the experimental PXRD patterns with those simulated by single crystal data, we are able to confirm the phase purity of the synthesized complexes. The three synthesized complexes were measured by PXRD, as shown below. The black, red and blue curves is correspond to the simulated sample, as-synthesized sample and the sample after vapor adsorption process, respectively.

From the PXRD of complex **1**, the as-synthesized pattern is consistent with the simulated data, confirming that the complex **1** has good phase purity. After the vapor adsorption process, the peak position of the PXRD pattern did not alternate, indicating that it is stable and suitable for vapor adsorption.

Similarly, from the PXRD of complex **2**, the as-synthesized pattern is consistent with the after vapor adsorption pattern.

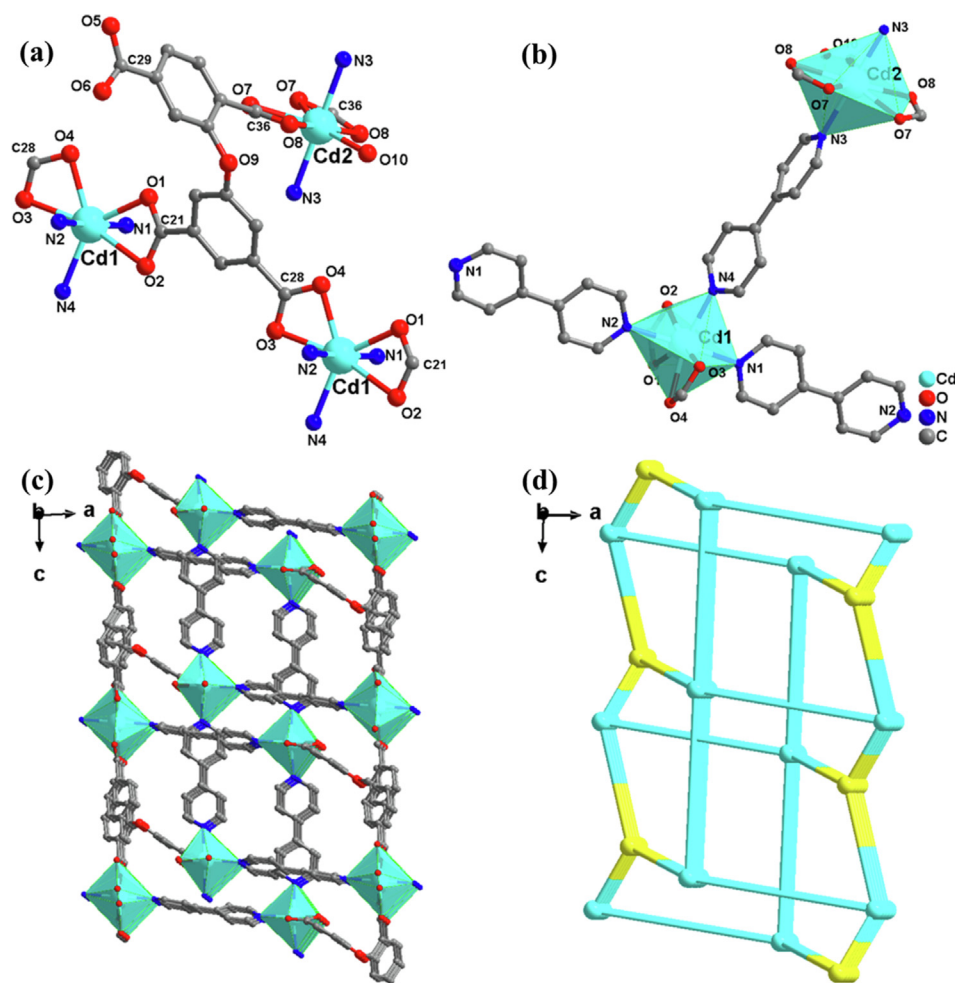


Fig. 2 (a) SBU of **2**; (b) Coordination circumstance of the Cd atom in **2**; (c) 3D framework along c axis; (d) **pcu** topological network.

However, from Fig. S1(b), the simulated data peak is left-shifted compared with the other blue and black curves. Because complex **2** is highly flexible packing, its lattice constantly shrinks, causing the peak position to shift to the right (Lin et al., 2014; Chen et al., 2020).

In the PXRD results of complex **3**, the simulated curve is markedly different from the other two curves. As we can see from Fig. S1(c), PXRD can only present peaks of metal clusters. This is because the pores of the synthesized MOF are huge, and the electrons of C, O and N elements are much less than those of metal elements, leading to the weak diffraction peaks of these elements, which cannot present in the graph.

It can be seen from the thermogravimetry and derivative thermogravimetry (TG-DTG) (see Fig. S2) curve, that the original compounds **1** and **3** lose coordination water and lattice water molecules at about 180 °C. It is two stages of water loss of **2**, respectively at 110 °C and 300 °C. The structure of the desolvated samples remained stable until 400 °C, indicating that the three compounds could work stably within 400 °C.

The three synthesized complexes were analyzed by FT-IR spectrum, as shown in Fig. S3. The black, red and blue curves correspond to complexes **1**, **2** and **3**, respectively. It can be seen that the spectrums of the samples with auxiliary ligands are obviously different. From the curves, the wide absorption peak at 3400 cm⁻¹ is the stretching vibration peak of N—H,

indicating the presence of vinyl in **2** and **3**. There are three absorption peaks near 1600, 1500 and 1450 cm⁻¹ of the benzene ring, which are the C=C stretching vibration of aromatic hydrocarbon. Meanwhile, the absorption peak at 3030 cm⁻¹ is the unique C—H stretching vibration peak of the aromatic ring. At the same time, it is found that 1600 cm⁻¹ absorption bands split into two absorption bands of 1570 and 1610 cm⁻¹, indicating that the benzene ring has π - π conjugation with unsaturated groups or p - π conjugation with substituents containing lone pair electrons. There are oxygen atoms in the binding molecular formula. There is no strong absorption peak in the double bond region in the figure, indicating that there is no C=O double bond, indicating that O and Cd coordinate to form a Cd—O bond.

3.3. Adsorption properties

The special pore prompted us to study the adsorption of H₂O and alcohol at their corresponding vapor pressures and 293 K. ($P_0 = 2.09$ kPa for H₂O, 11.62 kPa for MeOH, 5.30 kPa for EtOH). As-synthesized samples of **1**, **2** and **3** immersed in CH₂Cl₂ for 48 h, and then heated to 105 °C for eight hours to obtain activated samples.

H₂O adsorption isotherm of **1**, **2** and **3** possess maximum adsorption capacity of 91.04, 84.61 and 260.08 cm³g⁻¹ at $P/P_0 = 0.9$.

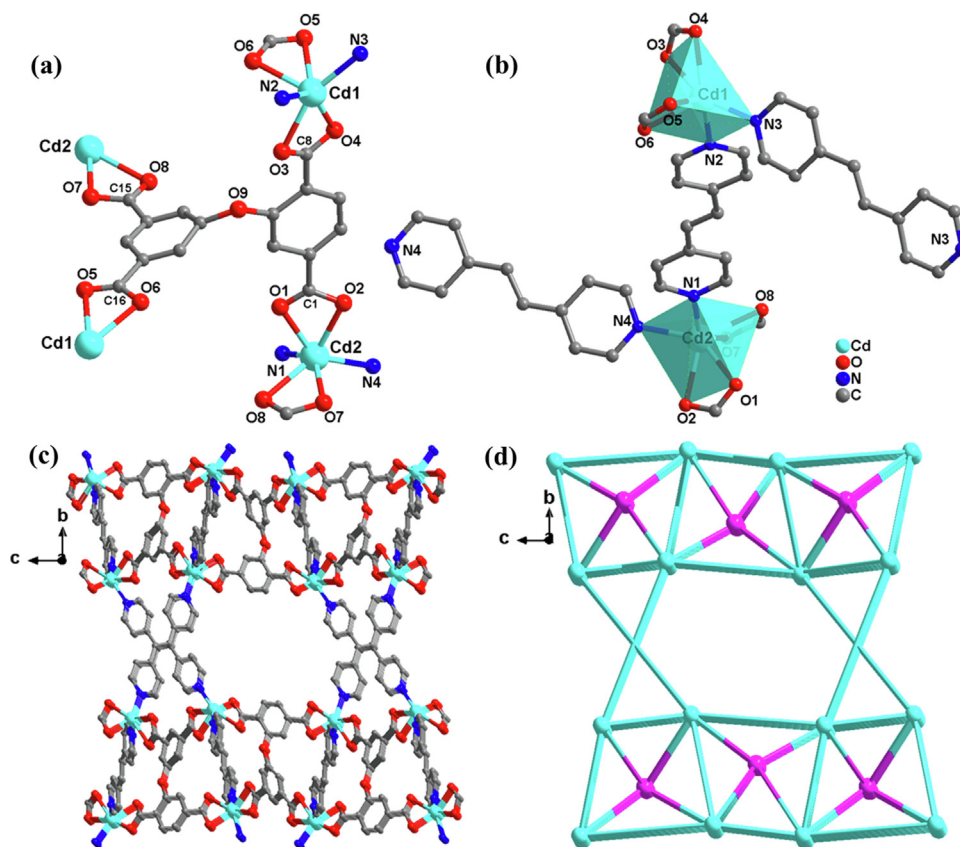


Fig. 3 (a) secondary building unit of **3**; (b) Coordination circumstance of the Cd atom in **3**; (c) 3D framework along the *a* axis; (d) topological network.

$P_0 \approx 1$, as shown in Fig. 4. However, they offer entirely different adsorption states. **1** is type-II isotherm, **2** is type-IV isotherm, and **3** is type-V isotherm. (See Fig. 4).

There are two steps in the H_2O adsorption isotherm of **1**: the first step appear at $P/P_0 < 0.5$, the loadings increase with relative pressure, isotherm convex upward; as the relative pressure increases, multi-layer adsorption begins to emerge. At saturation vapor pressure, the adsorption layers are infinite. This type-II profile of H_2O satisfies the BET model.

The adsorption isotherm of **2** shows a two staircase. The first stair is at $P/P_0 < 0.45$, and the second stair saturated at $P/P_0 \approx 1$. This type-IV profile is because **2** surface has mesopores and macropores- H_2O capillary coalescence occurs on the **2** surface when relative pressure at $P/P_0 = 0.4$. At high pressure, adsorption process appears only on the outer surface, which is much weaker than the inner surface. The curve tends to flatten.

The H_2O adsorption isotherm of **3** has three steps: the first step occurs at $P/P_0 < 0.25$, the adsorption capacity increases slowly with the relative pressure. The second step is about $P/P_0 < 0.85$, the adsorption capacity of H_2O increases rapidly. And the third step adsorption isotherm gradually tends to saturation. This V-shaped curve of H_2O may be due to the fact that the hydrophobic channel of **3** is composed of many hydrophobic benzene rings (Noll, 1987). In addition, large adsorption hysteresis loop is observed during the desorption.

The MeOH isotherms of **1** and **2** show type-II profiles. $P/P_0 < 0.05$, the adsorption capacity increased rapidly. And after P/P_0 greater than 0.8, there is a sharp increase. Then

following another sharp increase occurs near saturated vapor pressure and possesses adsorption amount of 110.67 and 68.28 cm^3g^{-1} , respectively. The sharp increase in P/P_0 close to 1 may be due to the capillary condensation phenomenon formed by the large pores generated by the accumulation of sample particles.

Isotherm of MeOH of **3** also shows a type-V profile just as H_2O on **3**. Firstly, the loading slowly rose at $P/P_0 < 0.2$, isotherm convex downward; and then, the adsorption capacity increases rapidly near $P/P_0 = 0.4$, and following the adsorption isotherm gradually saturates.

There are two main reasons for this result. Firstly, the multi-layer adsorption of MeOH on the hydrophobic surface of **3**. And secondly, the interaction between methanol and water is greater than the adsorption interaction with **3**, just like the adsorption of water vapor on the graphite surface (Huang et al., 2012).

At $P/P_0 \approx 1$, the absorption of EtOH by **1**, **2** and **3** is 24.57, 12.59 and 102.33 cm^3g^{-1} , respectively, and a delayed desorption isotherm is also observed, indicating an irreversible process. All of the three adsorption isotherms present type-I profiles. At $P/P_0 < 0.05$, the adsorption curve rises rapidly, and microporous adsorption occurs. The external surface adsorption occurs in the flat region. Both capillary coalescence and multi-layer adsorption will not happen. This is a classic Langmuir isotherm (Ayawei et al., 2017).

The adsorption capacity of H_2O and alcohol decreased with increasing molecular size, highlighting size-selective capture. Compared with **1** and **2**, the maximum adsorption capacity

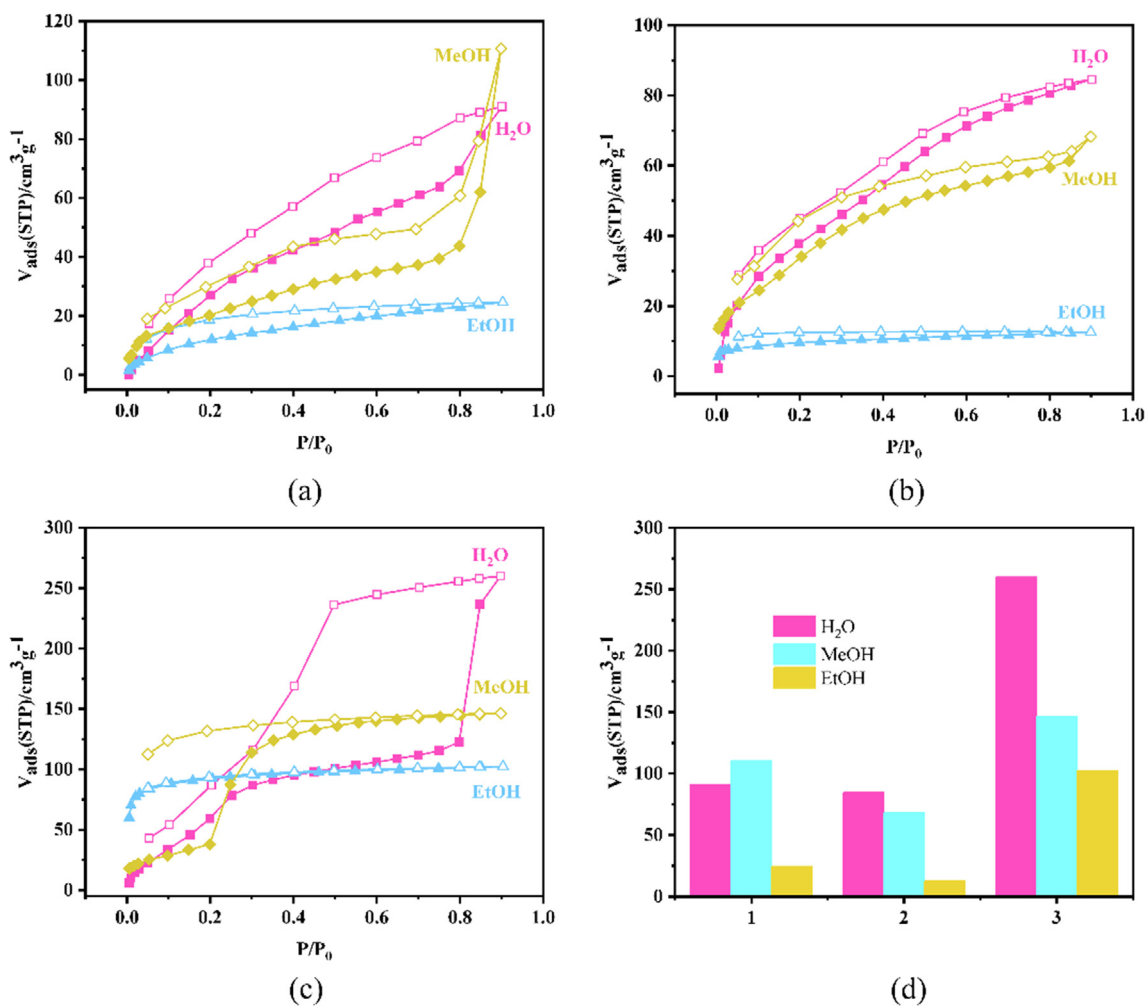


Fig. 4 Adsorptions-desorption isotherms of H₂O and alcohol vapor of (a)1, (b)2 and (c)3: H₂O, MeOH and EtOH at 293 K, where the filled and open shapes represent adsorption and desorption, respectively. (d) Comparison of maximum adsorption amounts.

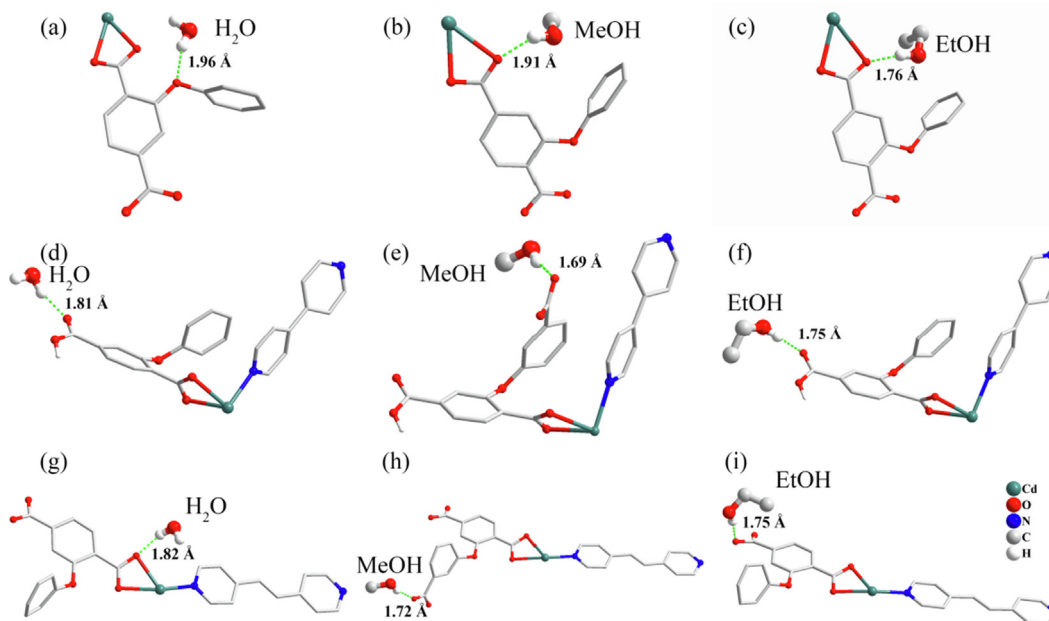


Fig. 5 Interactions between H₂O, MeOH and EtOH molecules and (a-c)1, (d-f)2 and (g-i)3.

of **3** is more than four times and eight times that of **1** and **2**, highlighting the specific flexible structure with high surface area and macroporous adsorption.

3.4. Adsorption mechanism

In order to understand the specific adsorption phenomena, GCMC simulations are performed at 293 K and corresponding vapor pressure of H₂O and alcohols.

In **1**, all guests interact with coordinated carboxylate and bridge O atoms by intense O-H_{guest}...O_{host} hydrogen bonds (H...O = 1.96 Å for H₂O, H...O = 1.91 Å for MeOH and H...O = 1.76 Å for EtOH).

The **2** and **3** are in contact with H atom of H₂O and alcohols, generating stronger O-H_{guest}...O_{host} hydrogen bonds (**2**: H...O = 1.81 Å for H₂O, H...O = 1.69 Å for MeOH and H...O = 1.75 Å for EtOH; **3**: H...O = 1.82 Å for H₂O, H...O = 1.72 Å for MeOH and H...O = 1.75 Å for EtOH). The result revealed that the attractive interactions between guests and **2** is the most intense. However, as mentioned above, **2** has the lowest adsorption capacity. This is because the adsorption capacity is not only related to the interaction between the guest molecule and the adsorbents, but also the porosity (Chen et al., 2011; Lv et al., 2012). One detail that deserves attention, unlike **1** and **3**, is that in **2**, the hydrogen bond length of methanol is significantly shorter than that of water and ethanol. This result will have a non-negligible impact on the adsorption separation performance.

To further understand the adsorption separation mechanism for the separation of the three vapors, the vapor selectivity of H₂O, MeOH and EtOH are analyzed utilizing the Ideal Adsorption Solution Theory (IAST) (Bojdys, 2013; Myers and Prausnitz, 1965). Through acquired pure component adsorption isotherms, the Langmuir-Freundlich (L-F) model provides a better fit to the isothermal parameters (Babarao et al., 2007; Goetz et al., 2006). The fitting curves and parameters shows in the supplementary information (Fig. S4-S6, Table S1-S3).

The adsorption selectivity of **1**, **2** and **3** for the three components shows in Fig. 6. Compared with **1** and **3**, **2** interacts more strongly with MeOH molecules, resulting in significant MeOH selectivity over EtOH under the condition of H₂O: MeOH: EtOH = 0.33: 0.33: 0.33.

According to the Fig. 6, the adsorption selectivity of MeOH/EtOH is 1.74, 44.9 and 0.03 at 5 kPa, respectively (Myers and Prausnitz, 1965; Zhu et al., 2021). Therefore, **2** has the potential ability to purify MeOH, and conversely, **3** can be applied to purify EtOH. These results suggest that the interaction between guests and adsorbent is a crucial factor in selective separation rather than saturated adsorption capacity.

MeOH and EtOH selectivity are studied at different humidity in Fig S7. The selectivity changed significantly under different humidity of **1**, **2** and **3**. Moreover, adsorption density contours of H₂O, MeOH and EtOH in channels of **1**, **2** and **3** are show in Fig. S8. In **1**, guests all occupy the channel constructed by two DPETA ligands. However, in **2** and **3**, the adsorption density distribution is significantly different. In **2** and **3**, the H₂O molecules occupy more near the N atom of the pyridine ring attached to the Cd atom, while the methanol occupies more on the vinyl of the pyridine ring attached to the

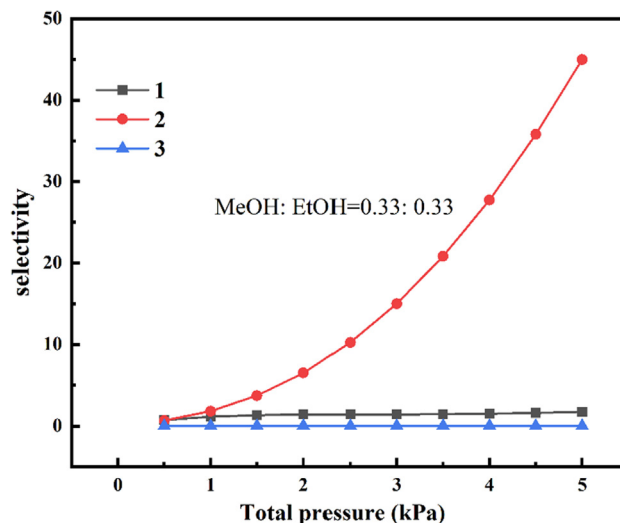


Fig. 6 Adsorption selectivity of **1**, **2** and **3** for three components mixture.

Cd atom. EtOH adsorbed on **2** near the Cd atom. On **3**, it adsorbs near the O bridge of the DPETA ligands. By comparison, it can infer that the vinyl group adjacent to N on the coordination pyridine ring has a good separation of MeOH and EtOH.

In **3**, H₂O and MeOH mainly adsorbed near N of pyridine atom linked to Cd atom. In contrast EtOH adsorbed near bridge O atom of DPETA under the combined interaction of carboxyl group and bridge O atom. Because the H...O is more robust than H...N. This is also the reason for the different adsorption selection ratios in **2** and **3**. And MeOH is adsorbed near the pyridine ring H by the combined interaction of the carboxyl group and the pyridine ring N atom (Castillo et al., 2008). This also demonstrates that modified **1** and the addition of a pyridine ligands can improve the adsorption of MOFs on MeOH.

This result enlightens us that the adsorption selectivity does not depend on the maximum adsorption amount of guests, but determines by the amount of adsorption in the flat or linear region (Lin et al., 2012). This also provides a favorable basis for the future preparation of screening MOFs suitable for separating specific substances.

4. Conclusions

We synthesized and modified three types of MOFs with DPETA ligands and auxiliary ligands. The increased vapor adsorption amount of H₂O and alcohol is observed in **3**, which has multi-layer adsorption and intense interaction between guests and MOFs. Owing to their particular structure and interaction sites, the modified MOFs show high selectivity adsorption of MeOH and EtOH under vapor state, suggesting possible application in capturing MeOH and EtOH from a mixture of ethanol and water or upgrading alcohol fuel.

5. Data availability

The data, models, and code used to support the findings of this study are available from the corresponding author upon request.

6. Funding statement

This research was funded by Medical Equipment Research Project, China (KJ2017A05193), Young Talent fund of University Association for Science and Technology in Shaanxi, China (20200608), NSF of Shaanxi Province, China (2021JQ-642) and NSF of Education Department of Shaanxi Province, China (21JK0687).

Declaration of Competing Interest

The authors declare the following financial interests/personal relationships which may be considered as potential competing interests: Xiuyuan Li reports financial support was provided by Institute of Scientific and Technical Information of Shaanxi. Chi Tang reports financial support was provided by Air Force Medical University.

Appendix A. Supplementary material

Supplementary data to this article can be found online at <https://doi.org/10.1016/j.arabjc.2022.104141>.

References

- Ayawei, N., Ebelegi, A.N., Wankasi, D., 2017. Modelling and interpretation of adsorption isotherms. *J. Chem.* 2017. <https://doi.org/10.1155/2017/3039817>.
- Babarao, R., Hu, Z., Jiang, J., Chempath, S., Sandler, S.I., 2007. Storage and separation of CO₂ and CH₄ in silicalite, C168 schwarzite, and IRMOF-1: a comparative study from Monte Carlo simulation. *Langmuir* 23. <https://doi.org/10.1021/la062289p>.
- Bojdys, M.J., 2013. Prediction of gas adsorption selectivity by ideal adsorption solution theory (IAST). *Comprehensive Manuals* 2.
- Castillo, J.M., Vlugt, T.J.H., Calero, S., 2008. Understanding water adsorption in Cu - BTC metal - organic frameworks. *J. Phys. Chem. C* 112. <https://doi.org/10.1021/jp806363w>.
- J. Chen, Y. Li, J. Gu, M. v. Kirillova, A.M. Kirillov, Introducing a flexible tetracarboxylic acid linker into functional coordination polymers: synthesis, structural traits, and photocatalytic dye degradation, *New Journal of Chemistry*. 44 (2020) 16082–16091. <https://doi.org/10.1039/D0NJ03628E>.
- Chen, M.S., Wang, H., Takamizawa, S., Okamura, T.A., Fan, J., Sun, W.Y., 2011. Single-crystal-to-single-crystal transformations and selective adsorption of porous copper(II) frameworks. *Chem. Commun.* 47, 3787–3789. <https://doi.org/10.1039/C0CC04689B>.
- Decoste, J.B., Peterson, G.W., Schindler, B.J., Killops, K.L., Browe, M.A., Mahle, J.J., 2013. The effect of water adsorption on the structure of the carboxylate containing metal-organic frameworks Cu-BTC, Mg-MOF-74, and UiO-66. *J. Mater. Chem. A* 1. <https://doi.org/10.1039/c3ta12497e>.
- Deng, J.H., Wen, Y.Q., Willman, J., Liu, W.J., Gong, Y.N., Zhong, D. C., Lu, T.B., Zhou, H.C., 2019. Facile exfoliation of 3D pillared metal-organic frameworks (MOFs) to produce MOF nanosheets with functionalized surfaces. *Inorg. Chem.* 58, 11020–11027. https://doi.org/10.1021/ACS.INORGCHEM.9B01564/SUP-PL_FILE/IC9B01564_SI_001.PDF.
- H.T. do Thi, P. Mizsey, A.J. Toth, Separation of Alcohol-Water Mixtures by a Combination of Distillation, Hydrophilic and Organophilic Pervaporation Processes, *Membranes* 2020, Vol. 10, Page 345. 10 (2020) 345. <https://doi.org/10.3390/MEMBRANES10110345>.
- Duan, L., Wu, Z.H., Ma, J.P., Wu, X.W., Bin Dong, Y., 2010. Adsorption and separation of organic six-membered ring analogues on neutral Cd(II)-MOF generated from asymmetric schiff-base ligand. *Inorg. Chem.* 49, 11164–11173. <https://doi.org/10.1021/ic101756t>.
- A.A. Fomkin, G.A. Petukhova, Features of Gas, Vapor, and Liquid Adsorption by Microporous Adsorbents, *Russian Journal of Physical Chemistry A* 2020 94:3. 94 (2020) 516–525. <https://doi.org/10.1134/S0036024420030097>.
- Goetz, V., Pupier, O., Guillot, A., 2006. Carbon dioxide-methane mixture adsorption on activated carbon. *Adsorption* 12, 55–63. <https://doi.org/10.1007/s10450-006-0138-z>.
- Guan, Q.L., Han, C., Bai, F.Y., Liu, J., Xing, Y.H., Shi, Z., Sun, L.X., 2020. Bismuth-MOF based on tetraphenylethylene derivative as a luminescent sensor with turn-off/on for application of Fe³⁺ + detection in serum and bioimaging, as well as emissive spectra analysis by TRES. *Sensors and Actuators, B Chem.* 325. <https://doi.org/10.1016/j.snb.2020.128767>.
- Huang, Z.H., Liu, G., Kang, F., 2012. Glucose-promoted Zn-based metal-organic framework/graphene oxide composites for hydrogen sulfide removal. *ACS Appl. Mater. Interfaces* 4. <https://doi.org/10.1021/am3013104>.
- Küsgens, P., Rose, M., Senkovska, I., Fröde, H., Henschel, A., Siegle, S., Kaskel, S., 2009. Characterization of metal-organic frameworks by water adsorption. *Micropor. Mesopor. Mater.* 120. <https://doi.org/10.1016/j.micromeso.2008.11.020>.
- Li, Y.W., Li, J., Wan, X.Y., Sheng, D.F., Yan, H., Zhang, S.S., Ma, H.Y., Wang, S.N., Li, D.C., Gao, Z.Y., Dou, J.M., Sun, D., Ma, H.Y., Wang, S.N., Sun, D., 2021. Nanocage-based N-rich metal-organic framework for luminescence sensing toward Fe³⁺ and Cu²⁺ ions. *Inorg. Chem.* 60, 671–681. <https://doi.org/10.1021/acs.inorgchem.0c02629>.
- Li, X.Y., Song, Y., Xiang, D., He, C., 2020. Promoted H₂O and alcohols adsorption performances by modifying the channel of MOF with uncoordinated N atom. *Inorg. Chem. Commun.* 122. <https://doi.org/10.1016/J.INOCHE.2020.108295>.
- Lin, Z.J., Lü, J., Hong, M., Cao, R., 2014. Metal-organic frameworks based on flexible ligands (FL-MOFs): structures and applications. *Chem. Soc. Rev.* 43, 5867–5895. <https://doi.org/10.1039/C3CS60483G>.
- Lin, Z., Zou, R., Liang, J., Xia, W., Xia, D., Wang, Y., Lin, J., Hu, T., Chen, Q., Wang, X., Zhao, Y., Burrell, A.K., 2012. Pore size-controlled gases and alcohols separation within ultramicroporous homochiral lanthanide-organic frameworks. *J. Mater. Chem.* 22, 7813–7818. <https://doi.org/10.1039/C2JM16324A>.
- Ling, Y., Chen, Z.X., Zhai, F.P., Zhou, Y.M., Weng, L.H., Zhao, D. Y., 2011. A zinc(II) metal-organic framework based on triazole and dicarboxylate ligands for selective adsorption of hexane isomers. *Chem. Commun.* 47, 7197–7199. <https://doi.org/10.1039/C1CC12253C>.
- Liu, G.C., Li, Y., Chi, J., Xu, N., Wang, X.L., Lin, H.Y., Chen, Y.Q., 2020. Multi-functional fluorescent responses of cobalt complexes derived from functionalized amide-bridged ligand. *Dyes Pigm.* 174. <https://doi.org/10.1016/j.dyepig.2019.108064>.
- Lu, Z., Luo, W., Huang, X., Yu, H., Li, Z., Liu, G., Liu, J., Chen, X., 2022. Highly-stable cobalt metal organic framework with sheet-like structure for ultra-efficient water oxidation at high current density. *J. Colloid Interface Sci.* 611, 599–608. <https://doi.org/10.1016/j.jcis.2021.12.132>.
- Lv, G.C., Wang, P., Liu, Q., Fan, J., Chen, K., Sun, W.Y., 2012. Unprecedented crystal dynamics: reversible cascades of single-crystal-to-single-crystal transformations. *Chem. Commun.* 48, 10249–10251. <https://doi.org/10.1039/C2CC35456J>.
- Myers, A.L., Prausnitz, J.M., 1965. Thermodynamics of mixed-gas adsorption. *AIChE J.* 11, 121–127. <https://doi.org/10.1002/aic.690110125>.
- Noll, L.A., 1987. Adsorption of aqueous benzene onto hydrophobic and hydrophilic surfaces. *Colloids Surf.* 28, 327–329. [https://doi.org/10.1016/0166-6622\(87\)80193-2](https://doi.org/10.1016/0166-6622(87)80193-2).

- Sakata, Y., Furukawa, S., Kondo, M., Hirai, K., Horike, N., Takashima, Y., Uehara, H., Louvain, N., Meilikhov, M., Tsuruoka, T., Isoda, S., Kosaka, W., Sakata, O., Kitagawa, S., 1979. Shape-memory nanopores induced in coordination frameworks by crystal downsizing. *Science* 339 (2013), 193–196. <https://doi.org/10.1126/SCIENCE.1231451>.
- Sander, U., Soukup, P., 1988. Design and operation of a pervaporation plant for ethanol dehydration. *J. Membr. Sci.* 36, 463–475. [https://doi.org/10.1016/0376-7388\(88\)80036-X](https://doi.org/10.1016/0376-7388(88)80036-X).
- Schoenecker, P.M., Carson, C.G., Jasuja, H., Flemming, C.J.J., Walton, K.S., 2012. Effect of water adsorption on retention of structure and surface area of metal-organic frameworks. *Ind. Eng. Chem. Res.* 51. <https://doi.org/10.1021/ie202325p>.
- Schüttrumpf, A., Bulut, A., Hermer, N., Zorlu, Y., Kirpi, E., Stock, N., Yazaydin, A.Ö., Yücesan, G., Beckmann, J., 2017. From tetrahedral tetraphosphonic acids E[p-C6H4P(O)(OH)2]4 (E=C, Si) to porous Cu- and Zn-MOFs with large surface areas. *ChemistrySelect* 2, 3035–3038. <https://doi.org/10.1002/SLCT.201700573>.
- Selvaraj, M., Banat, F., 2019. Ethanol-water separation using membrane technology. *Biorefinery*, 211–232. https://doi.org/10.1007/978-3-030-10961-5_9.
- Sheldrick, G.M., 2015. Crystal structure refinement with SHELXL. *Acta Crystallograph. Sec. C, Struct. Chem.* 71, 3. <https://doi.org/10.1107/S2053229614024218>.
- Spek, A.L., 2003. Single-crystal structure validation with the program PLATON. *J. Appl. Crystallogr.* 36, 7–13. <https://doi.org/10.1107/S0021889802022112>.
- Wong-Ng, W., Culp, J., Siderius, D.W., Chen, Y., Wang, S.Y.G., Allen, A.J., Cockayne, E., 2021. Synthesis, structural and sorption characterization of a Hofmann compound, Ni(3-methy-4,4'-bipyridine)[Ni(CN)4]. *Polyhedron* 200. <https://doi.org/10.1016/J.POLY.2021.115132>.
- Yuan, S., Chen, Y.P., Qin, J.S., Lu, W., Zou, L., Zhang, Q., Wang, X., Sun, X., Zhou, H.C., 2016. Linker installation: engineering pore environment with precisely placed functionalities in zirconium MOFs. *J. Am. Chem. Soc.* 138, 8912–8919. https://doi.org/10.1021/JACS.6B04501/SUPPL_FILE/JA6B04501_SI_003.CIF.
- Zheng, X., Huang, Y., Duan, J., Wang, C., Wen, L., Zhao, J., Li, D., 2014. A microporous Zn(ii)-MOF with open metal sites: structure and selective adsorption properties. *Dalton Trans.* 43, 8311–8317. <https://doi.org/10.1039/c4dt00307a>.
- Zhu, B., Cao, J.W., Mukherjee, S., Pham, T., Zhang, T., Wang, T., Jiang, X., Forrest, K.A., Zaworotko, M.J., Chen, K.J., 2021. Pore engineering for one-step ethylene purification from a three-component hydrocarbon mixture. *J. Am. Chem. Soc.* 143, 1485–1492. https://doi.org/10.1021/JACS.0C11247/SUPPL_FILE/JA0C11247_SI_001.PDF.